Ion beam figuring with focused anode layer thruster

O. I. Girka[1*], K. I. Lee[1], Y. S. Choi[1], S. O. Jang[1**]

[1]*Institute of Plasma Technologies, Korea Institute of Fusion Energy, 37 Dongjangsan-ro, 54004 Gunsan-si, Jeollabuk-do, Republic of Korea*

**Present address: Max-Planck-Institut für Plasmaphysik, Boltzmannstraße 2, D-85748 Garching, Germany*

***Corresponding author: sojang@kfe.re.kr*

ABSTRACT

This work presents the peculiarities of cone ion beam formation with a focused anode layer thruster (TAL) and its application to silicon carbide (SiC) ion beam figuring. Modeling results of Lorentz E×B force distribution in the discharge gap are presented. 3D particle tracing for keV Ar ions is carried out for the first time in the beam drift region of TAL with magnetic lens. Extracted ion beam full width at half maxima is about 2 mm in the focal plane, where the SiC etching rate reaches 0.5 μm/min. The SiC sputter yields are measured as a function of the Ar ion impact energy and beam incidence angle. The maximum sputter yield of 2.8 atom/ion is observed at 45 degrees of the beam-sample angle for the Si targets. Furthermore, the maximum sputter yield value of 1.7 atom/ion is measured at 30 degrees of the beam-sample angle for the SiC targets. The novelty of present research is in the application of focused TAL keV Ar ion beam to the SiC ion beam figuring.

I. INTRODUCTION

Ion beam figuring for the final processing of ultra-precision optical elements first originated several decades ago. Ion beam sputtering was considered as a tool for optical elements milling/trimming/polishing in mid-1960s.[1] At that time, ion beam figuring was carried out with high energy (20 keV and above), low current (fraction of a milliampere), and narrow beam diameter (usually less than one millimeter). Low etching rates, ion implantation, and radiation damage were among the key problems of that approach.[2] Kaufman broad-beam ion source was applied for fused silica etching at the end of 1980s to provide high etching rates.[3] Thereafter, various ion beam figuring instruments based on inductively coupled plasma (ICP) or transformer coupled plasma (TCP), capacitively coupled plasma (CCP), cross-fields drift plasma (E×B), and electron cyclotron resonance (ECR) were developed and investigated.[4, 5] Electrodeless ion sources were considered as more favorable for ion beam figuring, due to the longer operation cycles and better performance

under reactive gas operation.[6] ICP or TCP ion sources took leading positions in the ion beam figuring industry.[5,7-8] However, high sputter erosion rates of the source components joining the discharge chamber due to higher plasma sheath potentials[6] still remain an undesired feature of this class of devices. A low plasma sheath potential is favorable for the ion source performance, because the radiofrequency (RF) power supplied to the source is mainly consumed by dissociation and ionization of the process gas. Simultaneously, only a little power is consumed for ion acceleration in the plasma sheath. Specifically, these ions can drive an excessive erosion of the grid system of the ion source, resulting in reduced lifetime and high beam pollution.[5, 9]

TALs are well-known for the high current efficiency as well as being robust in design.[10] With this approach, there are various applications ranging from space propulsion[11-14] to microelectronics thin films coatings/trimming[4,15-17] and even fusion material research.[18-21] This paper presents the results of SiC ion beam figuring with the focused TAL. Main design concepts to prevent electrode erosion, decrease target contamination and achieve high current density/efficiency are discussed. Particular Ar ion energy range in combination to the relatively high beam current as well as relatively small beam spot meets the requirements for high-speed extreme ultraviolet reflective material surface treatment.[22] In this paper, SiC etching profiles with Ar ion beam, SiC sputter yield dependence on the ion impact energy, and beam incident angle are presented. The application of focused Ar ion beam from TAL to the SiC ion beam figuring is the distinctive feature of the present research.

II. ION BEAM FORMATION SYSTEM

The ion beam formation system consists of two stages. In the first stage, the ion beam is extracted from the closed drift region of TAL with the tilted anode-cathode gap. In the second stage, the ion beam is compressed with a magnetic lens. The principal scheme is based on the previously investigated Falcon ion source design.[23,24] In order to improve the ion beam formation, reduce the electrodes erosion, and extend the lifetime of pure Ar beam generation, the modelling of both E×B force localization and ion trajectories in 3D non-uniform magnetic field is carried out.

A. Cross-fields force localization in tilted anode-cathode gap

Closed electron drift is launched between the positively biased anode and cathodes at the ground potential. Transverse magnetic field is generated by the superposition of two magnetic field coils. These two coils form the configuration of the magnetic field that is required for sustaining E×B discharge and further ion beam compression (Fig. 1). TAL differs from stationary plasma thrusters (SPT) due to a significantly larger portion of the potential drop in the anode sheath.[10] The discharge gap distance and shape are crucial for the efficiency and lifetime of TAL, because they determine the

anode layer size and localization.[25] Particle in cell (PIC) simulations were previously used to show an impact of discharge gap dimensions and shape on ion beam extraction.[25-29] For a particular case of ion beam figuring, an extracted ion beam current density is one of the highest priorities.[30] In order to increase the extracted ion current density, it is necessary to have a well-localized anode layer, in which the ionization and acceleration take place.

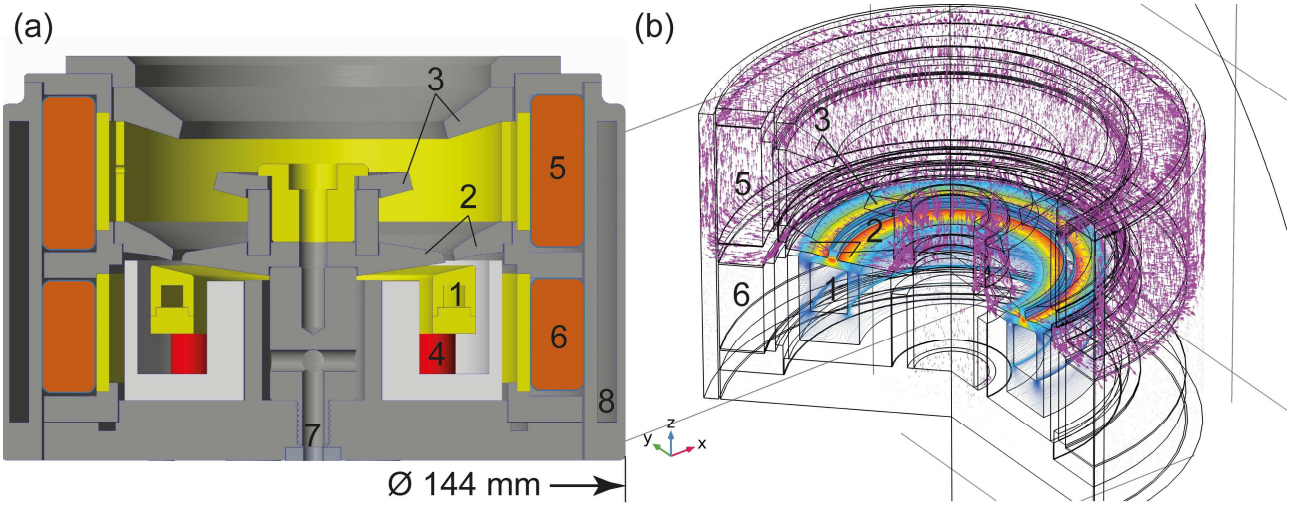

FIG. 1. Schematic of TAL with magnetic lens (a): 1 – anode, 2 – cathodes, 3 – magnetic lens, 4 – anode insulators, 5 – 250 turns coil, 6 – 150 turns coil, 7 – gas distributor channel, and 8 – coils water-cooling jacket; (b) magnetic field lines are shown with an array of magenta arrows. A magnetic field is a superposition produced by two magnetic field coils. Color chart shows the localization of E×B Lorentz force in the discharge gap.

In other words, the more intense and shrunk the anode layer is, the easier it is to control the beam with magnetic field and obtain a narrow resultant etching profile. Different versions of the discharge gap design are simulated in terms of the E×B force localization. The most beneficial configurations for the beam extraction are shown in Fig. 2. The strategy for the simulations is to make E×B layer (curvatures of electric and magnetic field lines) in the discharge gap as localized as possible. The smaller the anode layer, the smaller the high-voltage potential drop distance, the more neutrals are ionized and accelerated at the same point, the more ions gain the same energy, thereby facilitating the control of the beam with magnetic field. In our simulations, initially the curvature of magnetic fields in the cathode gap was the primary interest for particular ion gun dimensions and power requirements. Thereafter, the curvature of electric field lines is considered as the parameter in order to shrink the main ionization region. Under our experimental conditions, E×B force is localized in a 2.5 mm^2 area. It gives a narrow acceleration zone in a short potential drop and thin extracted circular beam. In Fig. 2(a), the configuration with “flat” anode-cathode configuration is shown, which provides well-concentrated D-shaped E×B force localization within the 2.5 mm2 region.

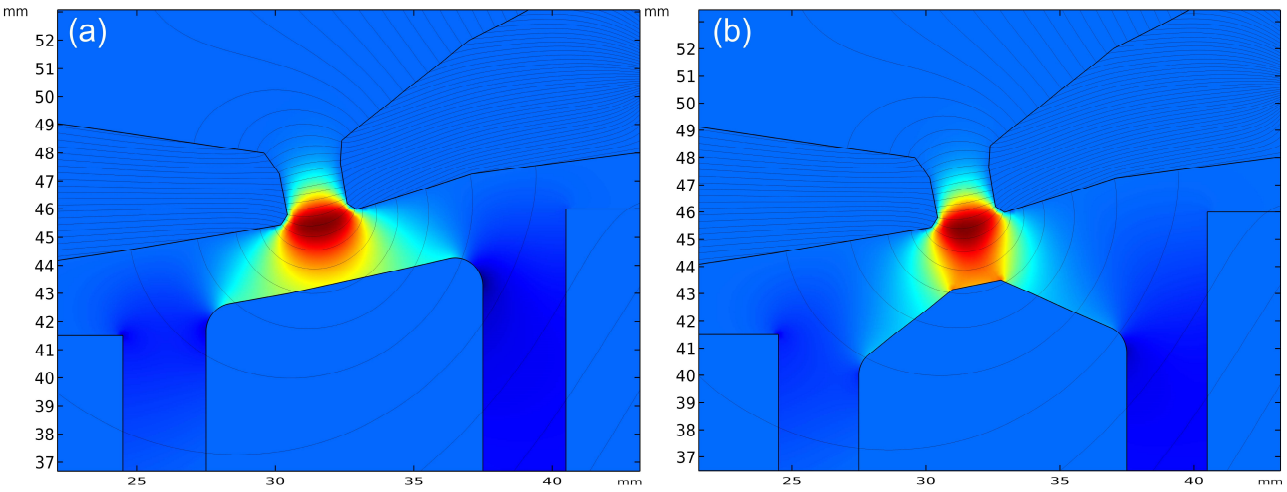

FIG. 2. Discharge gap with flat (a) and shaped (b) anode. Black bold lines show the discharge gap shape. Black thin lines are magnetic field lines. Color chart shows the distribution of E×B Lorentz force in arbitrary units.

The "shaped anode" configuration is shown in Fig. 2(b), which provides well-concentrated triangle-shaped E×B force localization with more uniform area near the anode surface. It gives a narrow acceleration zone in a short potential drop and thin extracted circular beam. Further magnetic focusing results in a cone-type beam formation and narrow beam profile.

B. Argon ion tracing in reversed magnetic field configuration

The ions, generated by impact ionization in E×B anode layer, are accelerated by the strong electric field. Afterwards, ions pass the area of strong magnetic field, which defines the curvature of their motion. The reversed magnetic field configuration minimizes the effect of transverse magnetic field and allows ions to reach the focal plane to form a well-concentrated ion beam.[23-24] Ion trajectory calculations for E×B systems were done in 3D with PIC simulations for cylindrical anode layer ion source without magnetic lens,[29] and analytical 1D approximation was carried out for the source with magnetic lens.[31] Variation in the ratio of magnetic field coil currents provided an adjustment of the beam focusing by means of the magnetic field fluxes ratio variation in the magnetic poles.[24] 3D Comsol particle tracing module is used in order to better understand the focused ion beam formation in the reversed magnetic field configuration. The simulations are carried out for two magnetic field coils with 150 and 250 turns, shown in Figs. 1 and 3. Specifically, two ratios are applied in Fig. 3 as limiting cases. The first combination in Fig. 3(a) shows the limiting case, when there is a negligibly small current of 0.5 A in the 250 turns coil and a relatively high current of 10 A in the 150 turns coil, and the beam is not focused at all. The second case in Fig. 3(b) shows the relatively high current of 10 A in the 250 turns coil and 3.5 A in the 150 turns coil to show that the beam is nicely focused.

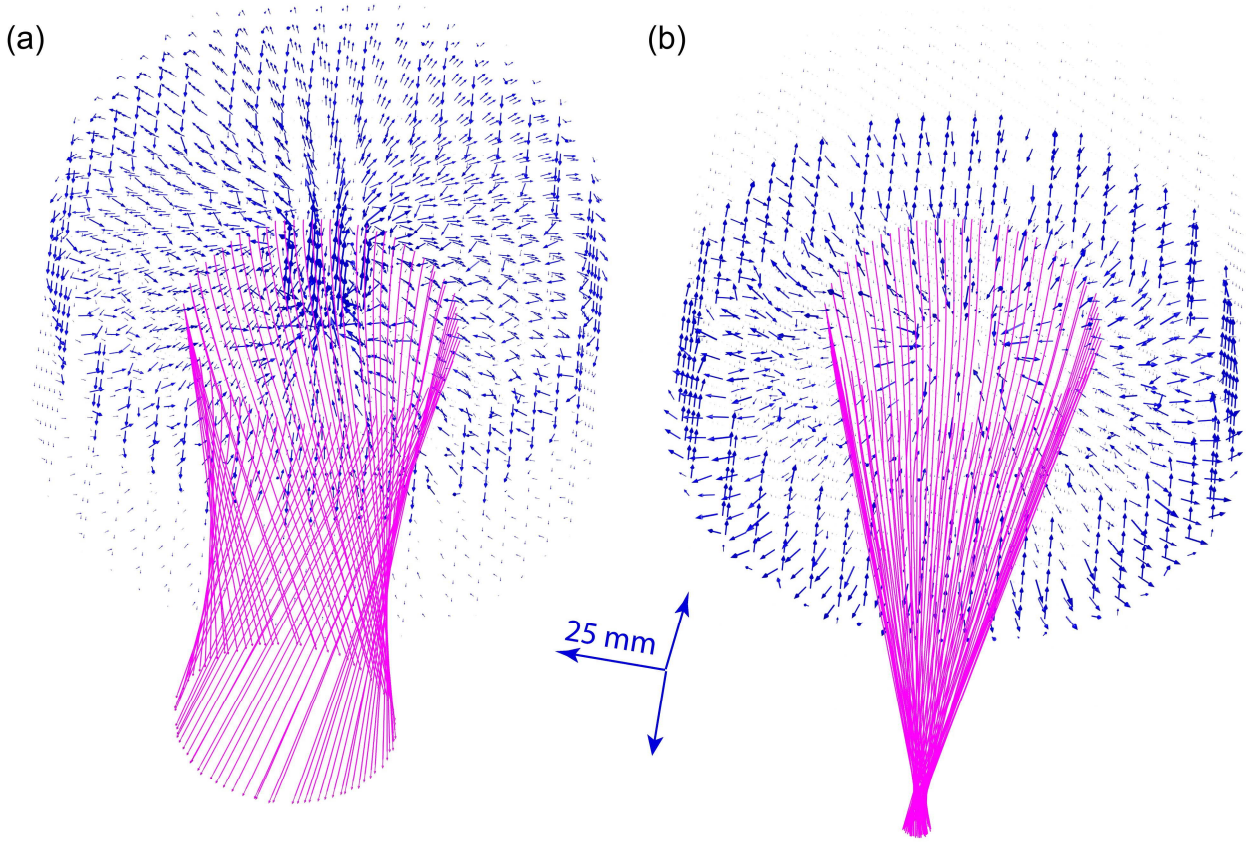

FIG. 3. Blue arrow array shows magnetic field lines, and magenta lines indicate 2 keV Ar ion trajectories for two different ratios of the currents in the magnetic field coils: (a) - 10 A are supplied to the coil with 150 turns and 0.5 A to the coil with 250 turns; (b) - 3.5 A are supplied to the coil with 150 turns and 10 A – to the coil with 250 turns.

One can see that the beam shape is well-controlled by the ratio of the magnetic field coil currents. TALs are well-known for the broad ion energy distribution function with the peak around 0.4 eU, where U is accelerating voltage and e is an elementary charge.[24] In order to observe the behavior of

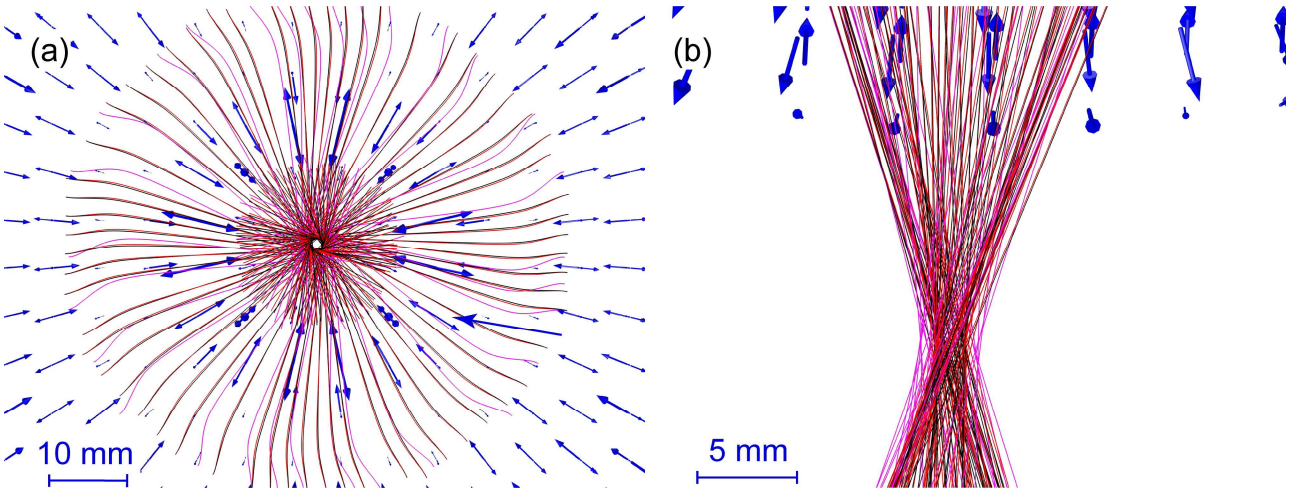

FIG. 4. Blue arrows show magnetic field lines. Magenta, red, and black lines indicate the trajectories of 0.5 keV Ar ions, 1 keV Ar ions, and 5 keV Ar ions. Fig. 4a shows the beam view from the focal plane and 4b – side view of ion trajectories at the focal plane.

ions in the focal plane, the simulations with the test Ar particles of 0.5, 1 and 5 keV are carried out. In Fig. 4 is the results of simulation when the beam is not perfectly focused. This mode allows achieving the resultant circular etching profile instead of the Gaussian profile.

III. EXPERIMENTAL SETUP

The experiments are carried out on the vacuum system equipped with 665 and 2000 l/s (for Ar) turbopumps. Vacuum system contains water-cooled Faraday cup having an aperture diameter of 8 mm, samples load lock and software-controlled target manipulator, shown in Fig. 5.

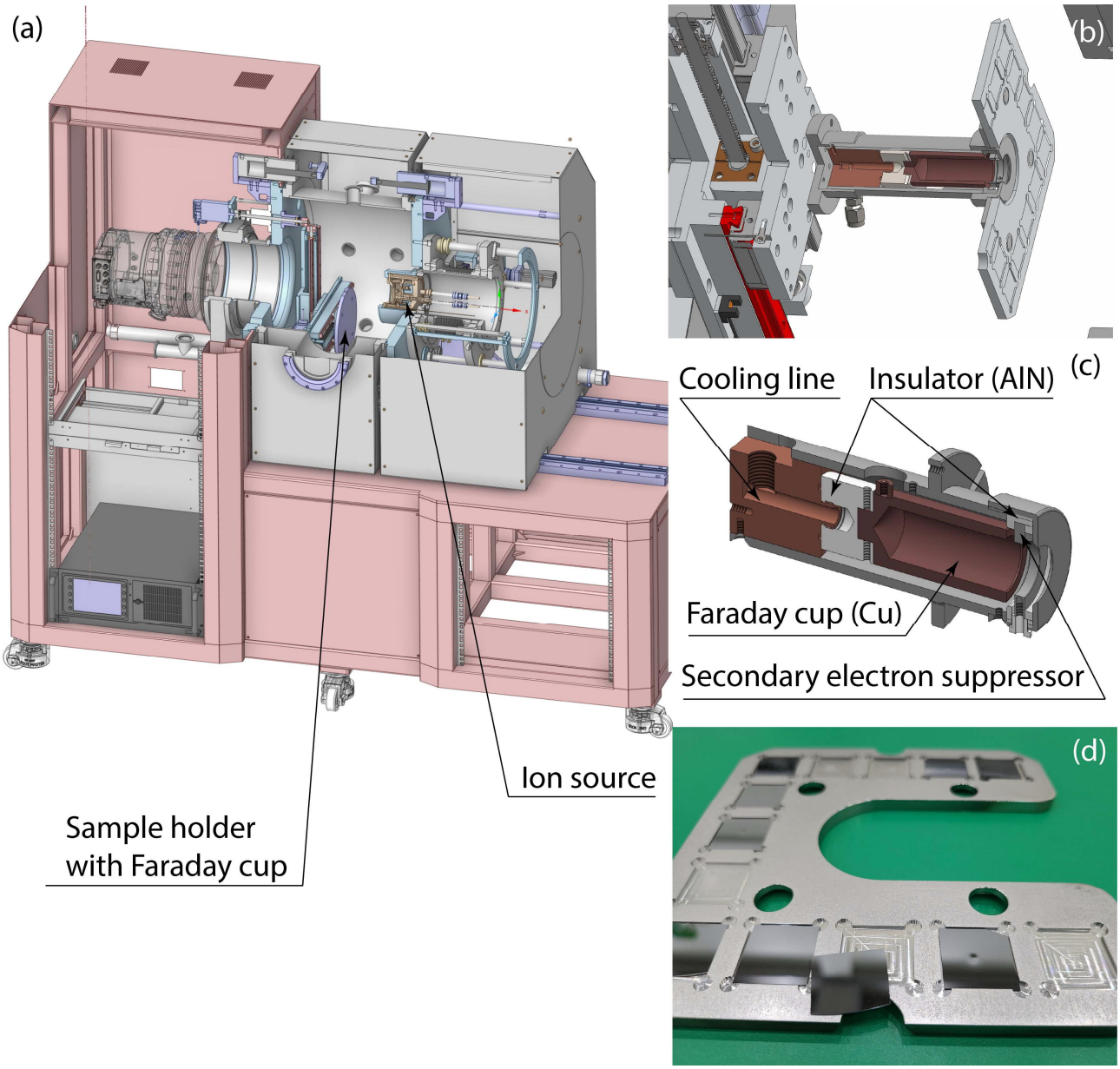

FIG. 5. Layout of full experimental setup. (a) IBF machine with two main components – ion source and movable sample holder with Faraday cup. (b) Sample holder and Faraday cup. (c) Cross-section of the Faraday cup. (d) Sample holder with etched Si sample.

Faraday cup is a central part of the movable sample holder mounted on the manipulator, shown in Fig. 5(b). Faraday cup consists of indirect water-cooled stainless steel housing, copper Faraday cup-receiver itself mounted on two AlN insulators, stainless steel secondary electron suppressor aperture, and 8 mm beam aperture in Fig. 5(c). Limiting pressure for the chamber reaches 2×10^{-7} Torr. Operating pressure for the source is 10^{-4}~10^{-5} Torr. The dependences of the operating pressure on the gas flow rate in Table I are for the pumping rates of 665 and 2000 l/s. The manufactured ion source is positioned at a distance of 10 cm from the target surface. During the etching experiments, the Gaussian-like beam etching profiles are obtained at a current of 4.5 A in the coil with 150 turns and at 10 A – in the coil with 250 turns. Coil current values are optimized during the experiment in order to obtain a narrower beam etching profile. The difference between the coils current values in the simulation and experiment is caused by imperfection in the coil winding. The accelerating voltage is varied from 1 to 5 kV. The discharge current is limited to 60 mA of the maximum current of the high-voltage power supply. Experiments are carried out using the wafer-type ultrafine polished Si and SiC samples. In order to have reliable repeatability and conduct a set of exposures within one experiment, a special sample holder for 13 samples (20 mm × 20 mm) is designed. Another sample holder is used for the angular sample irradiation, where the samples are positioned at 15, 30, 45, 75 and 90 degrees with respect to the beam symmetry axis. After the beam exposure the samples are analyzed using the Sartorius Lab Instruments micro-balance QUINTIX65-1SKR, NanoSystem NV-2400 optical profilometer, and Carl Zeiss Sigma scanning electron microscope (SEM) equipped with energy dispersive X-ray spectroscopy (EDS) analyzer from Thermo Scientific (Noran System 7 with ultra-dry silicon drift detector).

TABLE I. Dependences of operating pressure on gas flow rate for 665 and 2000 l/s pumping rates.

Flow rate	Pressure	
sccm	Torr	
	665 l/s	2000 l/s
0,5	8,20E-05	-
1	1,80E-04	1,10E-05
3	3,20E-04	3,40E-05
4	3,80E-04	-
5	-	5,80E-05
6	-	6,60E-05
7	-	7,40E-05
8	-	8,50E-05
9	-	9,80E-05

IV. RESULTS AND DISCUSSION

A. I-V curves and the source current efficiency

Faraday cup measurements of the current-voltage curves are carried out for the two pumping speed values. Previously,[17] a beam current extraction, i.e. a current efficiency was shown to strongly depend on the vacuum system performance in terms of the pumping rates. For example, for a 100 mm anode diameter, the current-voltage curves were compared for 300 and 1200 l/s for Ar, He and H.[32] For the present research with 63 mm anode diameter, the measurements are carried out for 665 and 2000 l/s for Ar, shown in Fig. 6 and 7.

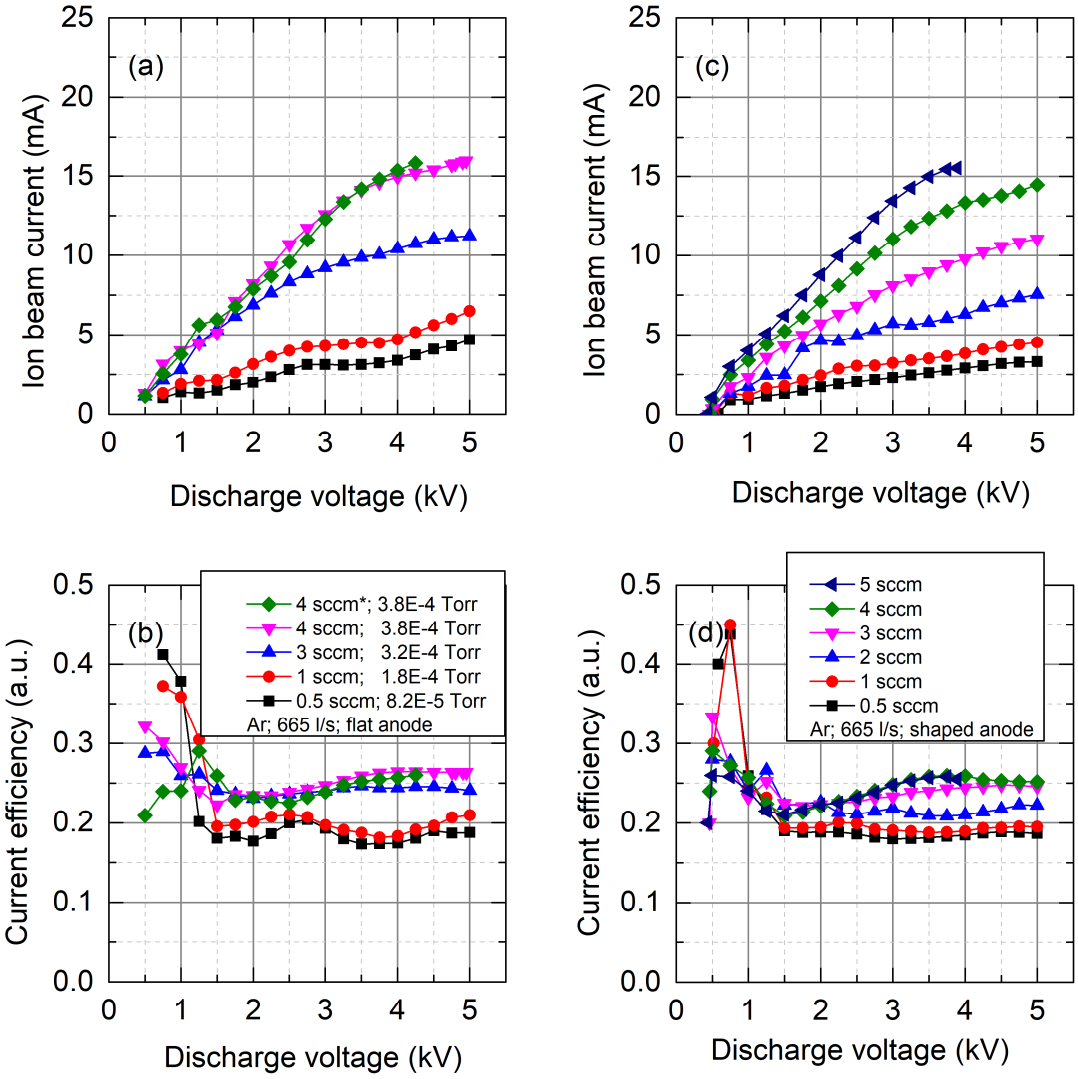

FIG. 6. Ion beam current and current efficiency (the ratio of the extracted ion beam current measured with Faraday cup to the discharge current measured with high-voltage DC power supply) as a function of discharge voltage for the flat (a, b) and shaped (c, d) anode configurations and 665 l/s pumping rate. "*" marked next to the 4 sccm curve in (a, b) corresponds to the case of 12 A and 5.4 A magnetic field coil current for comparison.

The total ion beam current is directly measured from the Faraday cup without bias voltage. In previous studies using similar ion beam system, the ion beam current measurements were carried out with biased target.[24] Results showed that unbiased target collects electrons from the beam region, which slightly underestimate the ion current measurements. The measurements are carried out for two discharge gap configurations in Fig. 5. The source shows current efficiency between 20 and 30% with Ar for the case of 665 l/s pump at higher discharge voltage values in Fig. 6. However, for the case of 2000 l/s, the source current efficiency almost reaches 40% even at intermediate discharge voltages in Fig. 7.

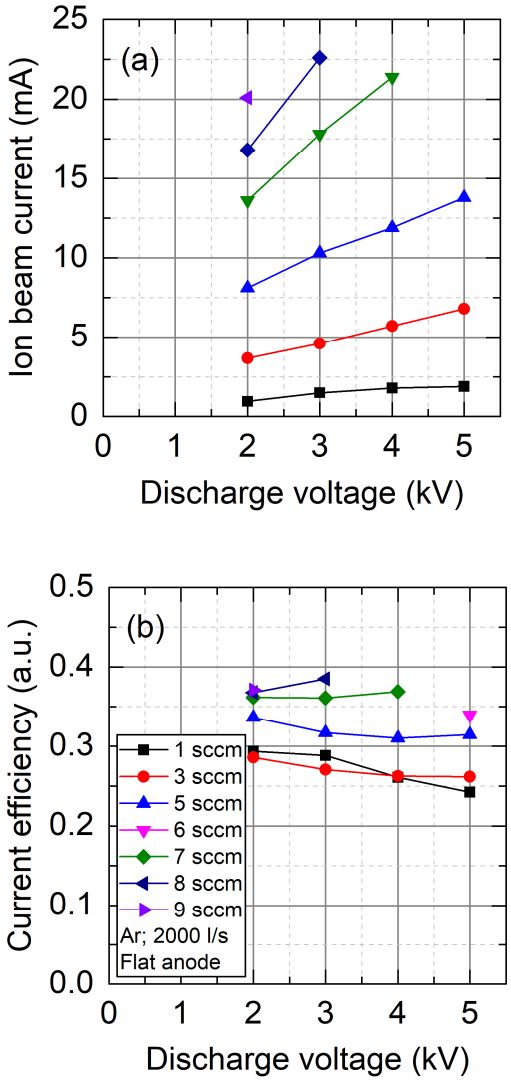

FIG. 7. Ion beam (a) and current efficiency (b) (the ratio of extracted ion beam current measured using the Faraday cup to the discharge current measured using the high-voltage DC power supply) as a function of the discharge voltage for the flat anode configuration and 2000 l/s pumping rate.

B. Surface contamination

Absence of surface contamination is a crucial point for the surface treatment instruments.[33] It is a strict requirement to keep the surface as clean as possible, especially when it comes to the ion beam figuring of the optical components. A set of samples is analyzed with SEM plus EDX after irradiation experiments. Minor Fe-containing clusters are considered to be the redeposition/exfoliation products of the Faraday cup, as soon as the surface and shape of the cathodes remain almost original after the half year (hundreds of hours) of operation. Most probably, these Fe, Si and C products are deposited in-between cathodes and magnetic lens poles and then are redeposited/exfoliated towards the sample surface. However, the possibility of cathode erosion cannot be completely excluded. The chemical composition of some exfoliated/redeposited flakes found on the SiC sample surface shows mostly the products of Si and C as expected for SiC etching experiments in Fig. 8.

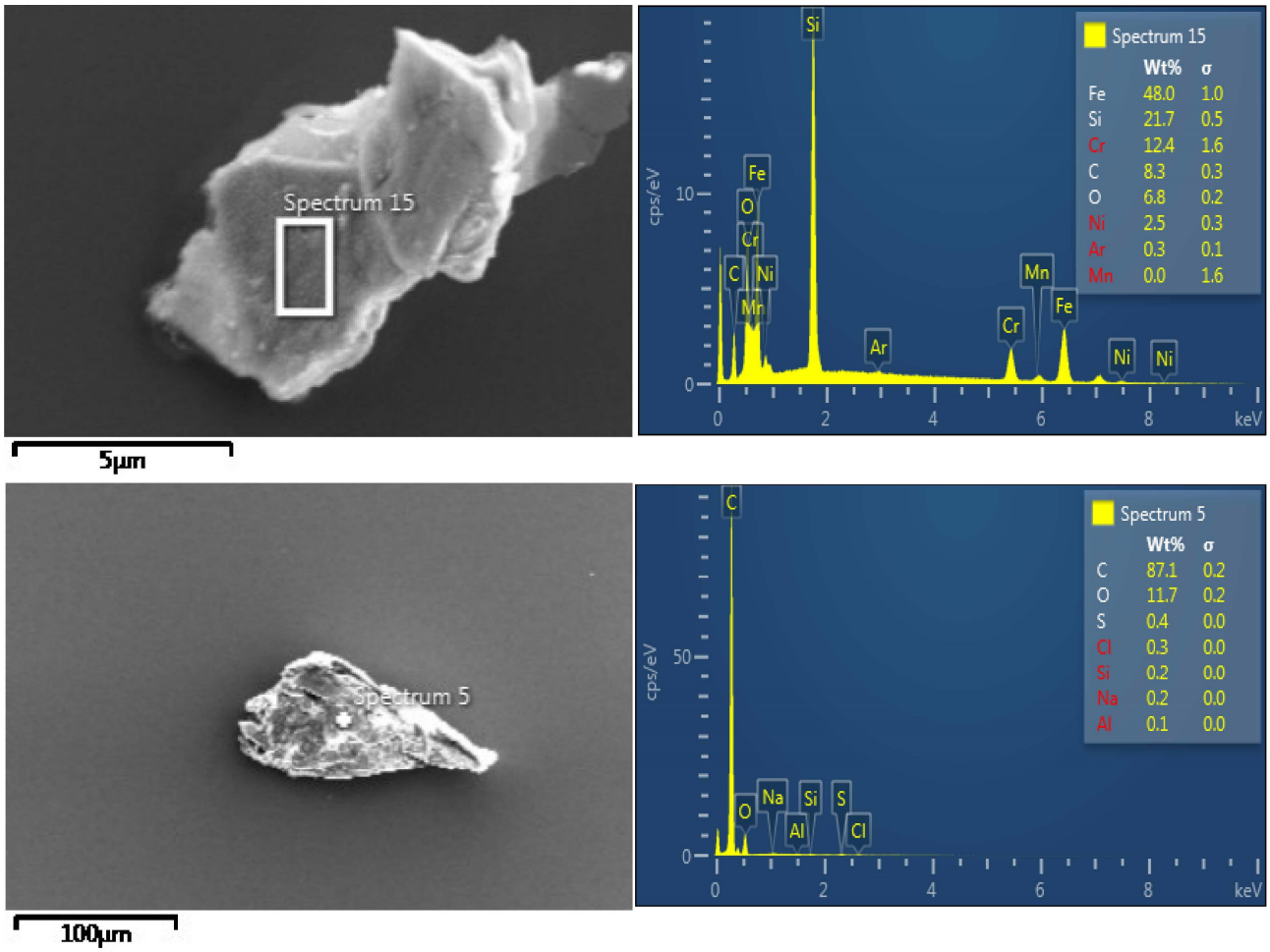

FIG. 8. Results of EDS examination of surface contamination. Fe, Si, and C clusters are found on the sample surfaces.

C. Etching profiles

Ultrafine polished SiC samples are irradiated with Ar ion beam at “normal” incidence angle in Fig. 9. The “normal” incidence angle is the angle between the beam symmetry axis and the target plane. One can see the bright light emission region at the axis of the beam symmetry. The formation of the compensating electron cloud was shown to be formed near the beam crossover region for a similar system in a previous study.[34] The ion current density measurements using Faraday probes for a Krypton Large Impulse Thruster were reported subsequently.[35] The ion beam divergence was proven to decrease with the discharge voltage increase even for the classical thruster without any magnetic lens. The increase in the discharge voltage leads to higher axial velocities for accelerated ions. As a result, the larger values of the ratio between the axial and transverse ion velocities lead to the smaller divergence of the beam,[35] which is a more favorable condition for focusing.

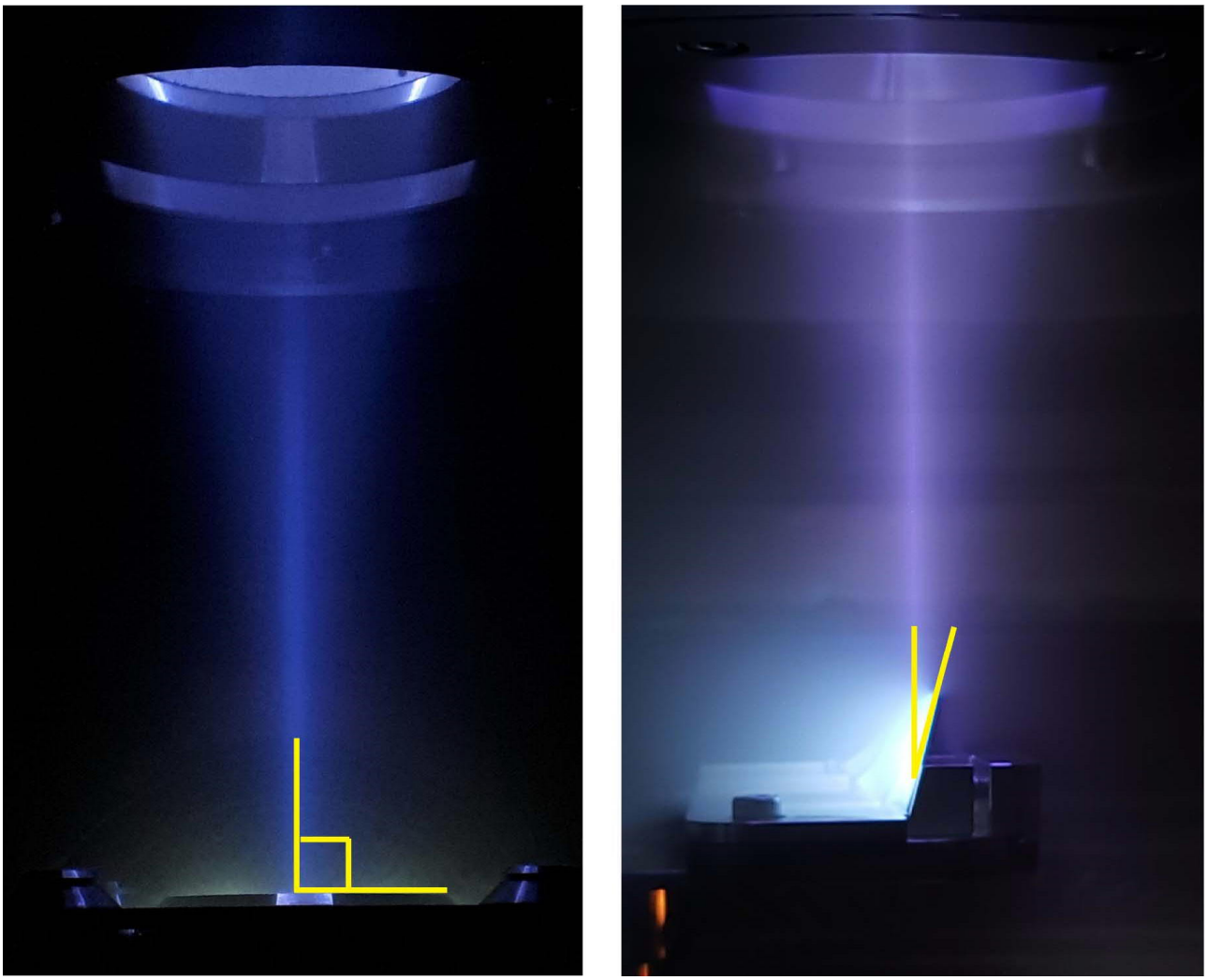

FIG. 9. Photo of the Ar ion beam drift region to Faraday cup at “normal” incidence angle (left), and to an inclined target (right).

As soon as an order of magnitude higher discharge voltage values (1~5 kV instead of 200~400 V) are used in the present research in combination with the magnetic lens, one can expect minor effects of beam divergence. Etching profiles show less than 2 mm full width at half maxima (FWHM) for the Gaussian-like shape in Fig. 10(a). Such a combination of FWHM and beam current results in a relatively high beam current density. One can introduce the following approximation for the beam current density:

$$j = j_0 \left(1 - \frac{r^2}{R^2}\right), \quad (1)$$

where j_0 is the maximum current density, r is the beam radius coordinate from 0 to beam radius R. Accordingly, the total current can be expressed[36] in the following form:

$$I = \int j\, ds = \int_0^R j(r) 2\pi r dr = \frac{\pi}{2} j_0 R^2. \quad (2)$$

From (2) one can get the expression for the maximum current density at the beam axis:

$$j_0 = \frac{2I}{\pi R^2}. \quad (3)$$

From Fig. 10(a), one can consider ~2 mm as the beam radius at a "foothill" of the etching profiles. Accordingly, the maximum current density at 5 mA of the total ion beam current reaches ~80 mA/cm^2. This estimation gives a comparatively high current density, which causes relatively high etching rate. Measured etching rate as a function of the ion energy (discharge voltage) shows close to linear growth and exceeds 0.5 μm/min for 5 kV discharge voltage and 5 mA of ion beam (Faraday cup) current in Fig. 10(b).

D. Angular dependence of etching rate

A comparison of experimental sputter yield to computational ones was reported previously for the CVD SiC and compared to Si for the incidence angle of 60 degrees with respect to the surface normal.[37-38] In order to benchmark our data for Si, and to cover the whitespace for SiC at different angles and ion energies, the angular dependence measurement of the sputter yield for ultrafine-polished Si and SiC wafers is carried out.

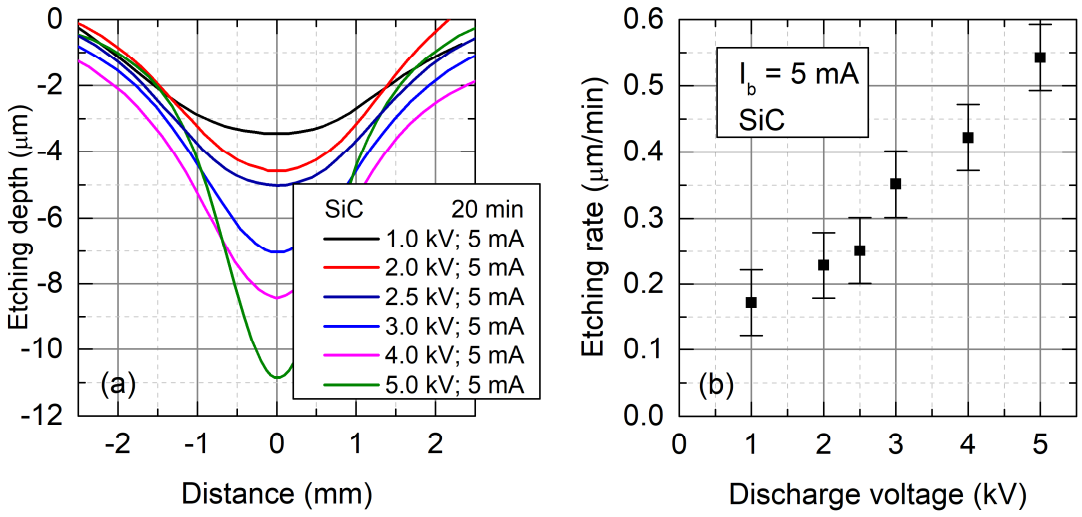

FIG. 10. Etching profiles of SiC samples with Ar ions at fixed beam current and irradiation time and different discharge voltage (ion energy) (a); etching rate as a function of discharge voltage (ion energy) at fixed beam current value (b).

Some of the previous reports on the Si and SiC etching were done with the use of end-Hall ion source and Xe, Kr, and Ar ions with the energy below 1 keV.[39] In the present research, the samples are positioned on the special sample holder at 15, 30, 45, 75 and 90 degrees with respect to the beam symmetry axis. A set of the samples is irradiated with Ar ions under the two experimental conditions during 20 minutes each. One set of conditions includes 1 keV irradiation - 2.5 kV of discharge voltage, 25 mA of discharge current, 5 mA of ion beam current, 2.0 sccm of Ar gas flow rate, operating pressure 1.3×10^{-4} Torr. The other set of conditions includes 2 keV irradiation - 5.0 kV of discharge voltage, 25 mA of discharge current, 5 mA of ion beam current, 0.5 sccm of Ar gas flow rate, operating pressure 7.5×10^{-5} Torr.

Etching rates are experimentally obtained with weight-loss measurement method. The sample weight is measured three times before and after ion irradiation experiments with Sartorius Lab Instruments micro-balance QUINTIX65-1SKR. Depending on the sample, weight is in the range 370~470 mg, while the weight loss is 0.9~3.4 mg, that is considerably more than microbalance precision: linearity is 0.1 mg and reproducibility is 0.02 mg. Error-bars are defined on the base of standard deviation of samples weight measurements. First, the sputter yield is measured as a function of the ion impact energy in Fig. 11(a). Ion energy distribution function for a similar system was measured previously with an electrostatic energy analyzer of spherical sector.[24] A set of experiments shows that 1 keV Ar ion energy provides the highest value of sputter yield for the defined energy range at a normal incidence angle. The experimental results on the Si and SiC angular sputter yield dependence are shown in Fig. 11(b). One can see that the sputter data are in a good agreement with the previously reported values for Si.[37, 38, 40] The sputtering yields obtained at 30 degrees under the

present experimental conditions are slightly smaller than the experimental ones obtained roughly by a factor of 1.4.[37] Such a difference might be caused by redeposition in the absence of masks that were used. This data deviation/scatter is acceptable in general for the sputter yield measurements.[38] However, the difference is almost negligible for the 90 degrees case, most probably because of the different directions of sputtered atoms flow.

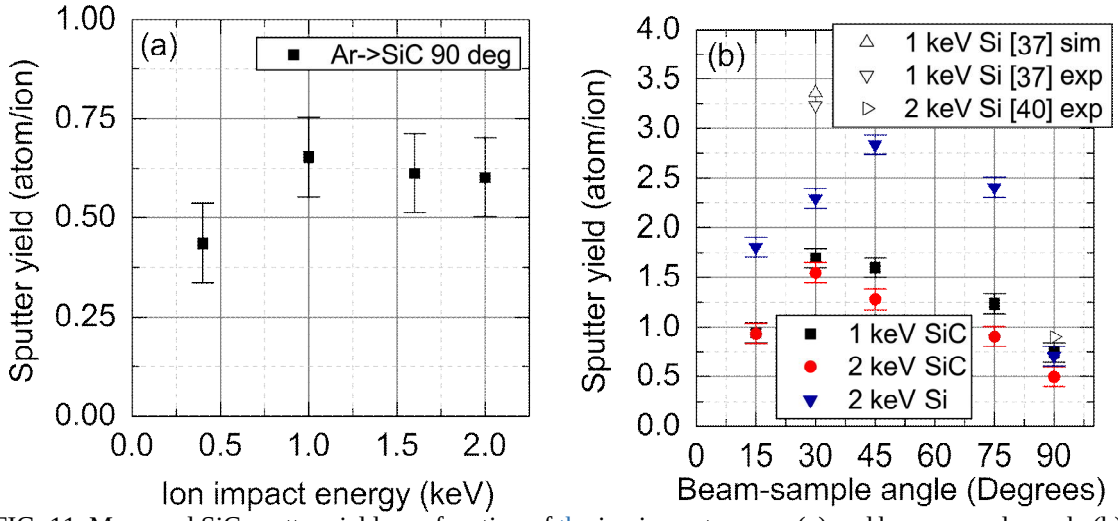

FIG. 11. Measured SiC sputter yield as a function of the ion impact energy (a) and beam-sample angle (b).

Most noticeable feature of the sputter yield angular dependence is that the maximum is clearly at 45 degrees for Si and at 30 degrees for SiC. These angles are also beneficial for the source contamination reduction with sputtered material: backflow of target sputtered particles is not directed completely towards the discharge gap region.

V. CONCLUSIONS

The peculiarities of cone ion beam formation with focused TAL are shown. The localization of E×B force and Ar ion tracing result in an improved extracted ion beam etching profile, which is crucial for the ion beam figuring application tasks. The resultant ion beam FWHM is approximately 2 mm and SiC etching rate reaches 0.5 μm/min. The investigation of the angular dependence of sputter yield shows the following. The maximum sputter yield of 2.8 atom/ion is at 45 degrees of the beam-sample angle for the Si targets. Furthermore, the maximum sputter yield value of 1.7 atom/ion is observed at 30 degrees of beam-sample angle for the SiC targets. TAL with magnetic lens can provide relatively high current density (~80 mA/cm^2 for this particular case), almost 40% current efficiency under the well-controlled DC power conditions without extraction grids. The ion energy range as well as the sort of the ion to target combination is proven to be suitable for surface

smoothening of Si and SiC components,[37, 39] Thus, the results are of interest for the surface treatment instrumentation of extreme ultraviolet reflective materials.

ACKNOWLEDGEMENTS

This research was supported by the R&D Program of 'Plasma Convergence & Fundamental Research' grant (EN2221) and 'Plasma Big-Data ICT Convergence Technology Research' grant (EN2242) through the Korea Institute of Fusion Energy (KFE) funded the Korea Ministry of Science and ICT (MSIT). The authors want to acknowledge and specially thank Dr. Kiyong Lee for his generous support and fruitful discussions.

Data Availability

The data that support the findings of this study are available from the corresponding author upon reasonable request.

References

[1] A. B. Meinel, S. Bashkin, and D. A. Loomis. Applied Optics **4**, 1674 (1965). https://doi.org/10.1364/AO.4.001674

[2] S. R. Wilson, D. W. Reicher, and J. R. McNeil. Proceedings of SPIE, Advances in Fabrication and Metrology for Optics and Large Optics **0966**, (1989). https://doi.org/10.1117/12.948051

[3] H. R. Kaufman and R. S. Robinson. Vacuum **39**, 1175 (1989). https://doi.org/10.1016/0042-207X(89)91116-0

[4] A. Anders. Surface and Coatings Technology **200**, 1893 (2005). https://doi.org/10.1016/j.surfcoat.2005.08.018

[5] T. Hänsel, F. Frost, A. Nickel, and T. Schindler. Vakuum in Forschung und Praxis **19**, 24 (2007). https://doi.org/10.1002/vipr.200700330

[6] H. Neumann, M. Tartz, F. Scholze, T. Chasse, H. Kersten, and H. Leiter. Contributions to Plasma Physics **47**, 487 (2007). https://doi.org/10.1002/ctpp.200710063

[7] T. Arnold and F. Pietag. Precision Engineering **41**, 119 (2015). http://dx.doi.org/10.1016/j.precisioneng.2015.03.009

[8] J. W. Kim, H. W. Cheong, Y. T. Hong, and K. W. Whang. Plasma Sources Science and Technology **26**, 035008 (2017). https://doi.org/10.1088/1361-6595/aa595e

[9] M. Zeuner, F. Scholze, B. Dathe, and N. Neumann. Surface and Coatings Technology **142–144**, 39 (2001). https://doi.org/10.1016/S0257-8972(01)01219-1

[10] E. Y. Choueiri. Physics of Plasmas **8**, 5025 (2001). https://doi.org/10.1063/1.1409344

[11] M. Keidar, I.D. Boyd, and I.I. Beilis. Physics of Plasmas **11**, 1715 (2004). https://doi.org/10.1063/1.1668642

[12] S. Mazouffre. Plasma Sources Science and Technology **25**, 033002 (2016). https://doi.org/10.1088/0963-0252/25/3/033002

[13] Y. Hamada, J. Bak R. Kawashima, H. Koizumi, K. Komurasaki, N. Yamamoto, Y. Egawa, I. Funaki, S. Iihara, S. Cho, K. Kubota, H. Watanabe, K. Fuchigami, Y. Tashiro, Y. Takahata, T. Kakuma, Y. Furukubo, H. Tahara. Transactions of the Japan Society for Aeronautical and Space Sciences **60**, 320 (2017). https://doi.org/10.2322/tjsass.60.320

[14] I. Levchenko, K. Bazaka, Y. Ding, Y. Raitses, S. Mazouffre, T. Henning, P.J. Klar, S. Shinohara, J. Schein, L. Garrigues, M. Kim, D. Lev, F. Taccogna, R.W. Boswell, C. Charles, H. Koizumi, Y. Shen, C. Scharlemann, M. Keidar, and S. Xu. Applied Physics Reviews **5**, 011104 (2018). https://doi.org/10.1063/1.5007734

[15]

[15] S. Mishin, Y. Oshmyansky, and F. Bi. IEEE International Frequency Control Symposium, 642 (2010). https://doi.org/10.1109/FREQ.2010.5556249

[16] A.A. Bizyukov, I.A. Bizyukov, O.I. Girka, K.N. Sereda, V.V. Sleptsov, M. Gutkin, and S. Mishin. Problems of Atomic Science and Technology **17**, 110 (2011). https://vant.kipt.kharkov.ua/ARTICLE/VANT_2011_1/article_2011_1_110.pdf

[17] O. Girka, A. Bizyukov, I. Bizyukov, M. Gutkin, and S. Mishin. Nukleonika **60**, 327 (2015). https://doi.org/10.1515/nuka-2015-0059

[18] V.A. Makhlaj, N.N. Aksenov, O.V. Byrka, I.E. Garkusha, A.A. Bizyukov, I.A. Bizyukov, O.I. Girka, K.N.Sereda, S.V. Bazdyreva, S.V. Malykhin, and A.T. Pugachov. Problems of Atomic Science and Technology. No. 1. Series: Plasma Physics **83**, 70 (2013). https://vant.kipt.kharkov.ua/ARTICLE/VANT_2013_1/article_2013_1_70.pdf

[19] S.S. Herashchenko, V.A. Makhlaj, O.I. Girka, N.N. Aksenov, I.A. Bizyukov, S.V. Malykhin, S.V. Surovitskiy, K.N. Sereda, and A.A. Bizyukov. Problems of Atomic Science and Technology, No. 6. Series: Plasma Physics **22**, 69 (2016). http://vant.kipt.kharkov.ua/ARTICLE/VANT_2016_6/article_2016_6_69.pdf

[20] S.S. Herashchenko, O.I. Girka, S.V. Surovitskiy, V.A. Makhlai, S.V. Malykhin, M.O. Myroshnyk, I.O. Bizyukov, N.N. Aksenov, S.S. Borisova, O.A. Bizyukov, and I.E. Garkusha. Nuclear Instruments and Methods in Physics Research Section B: Beam Interactions with Materials and Atoms **440**, 82 (2019). https://doi.org/10.1016/j.nimb.2018.12.010

[21] S.V. Malykhin, I.E. Garkusha, V.A. Makhlai, S.V. Surovitskiy, S.S. Herashchenko, and O.I. Girka. Nuclear Instruments and Methods in Physics Research B: Beam Interactions with Materials and Atoms **481**, 6 (2020). https://doi.org/10.1016/j.nimb.2020.08.013

[22] Y. Nakanishi, R. Mukai, S. Matsuyama, K. Yamauchi, and Y. Sano. Materials Science Forum **1004**, 161 (2020). https://doi.org/10.4028/www.scientific.net/MSF.1004.161

[23] M. Gutkin, A. Bizyukov, V. Sleptsov, I. Bizyukov, and K. Sereda, U.S. Patent US7622721B2 (2009). https://patents.google.com/patent/US7622721B2

[24] O. Girka, I. Bizyukov, K. Sereda, A. Bizyukov, M. Gutkin, and V. Sleptsov. Review of Scientific Instruments **83**, 083501 (2012). https://doi.org/10.1063/1.4740519

[25] S. Lee, J.-K. Kim, and D.-G. Kim. Review of Scientific Instruments **83**, 02B703 (2012). https://doi.org/10.1063/1.3665961

[26] I.D. Boyd. Journal of Propulsion and Power **16**, 902 (2000). https://doi.org/10.2514/2.5658

[27] S. Yasui, K. Kumakura, N. Yamamoto, K. Komurasaki, and Y. Arakawa. 39th AIAA/ASME/SAE/ASEE Joint Propulsion Conference and Exhibit, Session: EP-8: Hall Thruster Physics and Modeling I, 2003. https://doi.org/10.2514/6.2003-4702

[28] F. Taccogna, S. Longo, M. Capitelli, and R. Schneider. Computer Physics Communications **164**, 160 (2004). https://doi.org/10.1016/j.cpc.2004.06.025

[29] P. Li, F. Zhang, S. Geng, J. Zhao, and D. Tang. Surface and Coatings Technology **365**, 102 (2019). https://doi.org/10.1016/j.surfcoat.2018.08.059

[30] Y.-S. Ho and Y.-S. Hwang. Patent KR20140128140A, 2014. https://patents.google.com/patent/KR20140128140A

[31] O.I. Girka, I.O. Bizyukov, O.A. Bizyukov, K.M. Sereda, and O.V. Romashchenko. Uzhhorod University Scientific Herald. Series Physics **30**, 45 (2011). https://dspace.uzhnu.edu.ua/jspui/handle/lib/6461

[32] O. Girka, O. Bizyukov, Yu. Kolyada, K. Sereda, and I. Bizyukov. Problems of Atomic Science and Technology **98**, 22 (2015). http://vant.kipt.kharkov.ua/ARTICLE/VANT_2015_4/article_2015_4_22.pdf

[33] K.-I. Lee, D. C. Seok, S. O. Jang, and Y. S. Choi. Thin Solid Films **707**, 1380842 (2020). https://doi.org/10.1016/j.tsf.2020.138084

[34] A. A. Bizyukov, O. I. Girka, E. V. Romashchenko, K. N. Sereda, and N. N. Yunakov. Problems of Atomic Science and Technology **83**, 204 (2013). https://vant.kipt.kharkov.ua/ARTICLE/VANT_2013_1/article_2013_1_204.pdf

[35] A. Szelecka, M. Jakubczak, and J. Kurzyna. Laser and Particle Beams **36**, 219 (2018). https://doi.org/10.1017/S0263034618000198

[36] D. Filippetto, P. Musumeci, M. Zolotorev, and G. Stupakov. Physical Review Accelerators and Beams **17**, 024201 (2014). http://dx.doi.org/10.1103/PhysRevSTAB.17.024201

[37] G. Ecke, R. Kosiba, V. Kharlamov, Y. Trushin, and J. Pezoldt. Nuclear Instruments and Methods in Physics Research Section B: Beam Interactions with Materials and Atoms **196**, 39 (2002). https://doi.org/10.1016/S0168-583X(02)01273-9

[38] R. Behrisch, W. Eckstein (Eds.), Springer, Berlin, 2007. https://doi.org/10.1007/978-3-540-44502-9

[39] P. Gailly, J. -P. Collette, C. Jamar, K. Fleury-Frenette, P. Medart, and Y. Stockman. Nuclear Instruments and Methods in Physics Research Section B: Beam Interactions with Materials and Atoms **216**, 206 (2004). https://doi.org/10.1016/j.nimb.2003.11.036

[40] K. Wittmaack and D. B. Poker. Nuclear Instruments and Methods in Physics Research Section B: Beam Interactions with Materials and Atoms **47**, 224 (1990). https://doi.org/10.1016/0168-583X(90)90750-O